corrosion and materials degradation

MDPI

Article

Passive Oxide Destruction by Dense Low-Energy Radionuclide i-Analyzed by Voltammetry ii-Analyzed by Chaos

Gilbert Bellanger

Independent Researcher, 21260 Selongey, France; gilbert.bellanger@orange.fr; Tel.: +33-(1)-380-757-610

Abstract: The destruction of the passive oxide can be caused by the action of a radionuclide, which collides with the surface of the oxide. In this case, the β^- nuclear particle produced by the decay of tritiated water is considered for corrosion, and it follows that the β^- energy is absorbed first into the oxide. The penetration depth is sufficient for all the passive oxides to be destabilized. Destabilization was examined by voltammetry and by the electrochemical circuit in the passive potential. The corresponding pathway leads to the destruction of oxide. Tests carried out using a chaos data analyzer are an aid for expertise. Different behavior may occur depending on the passive potential and the β^- density. The synchronization of phase space spectra and tests realized sector by sector make possible the interpretation of divergence leading to unstable oxide and oxide destruction at different passive potentials and for different β^- particle densities.

Keywords: voltammetry; chaos analysis; β^- radiation energy; passive oxide; unstable oxide

Citation: Bellanger, G. Passive Oxide Destruction by Dense Low-Energy Radionuclide i-Analyzed by Voltammetry ii-Analyzed by Chaos. *Corros. Mater. Degrad.* **2023**, *4*, 398–427. https://doi.org/10.3390/cmd4030021

Academic Editor: Angeliki G. Lekatou

Received: 26 April 2023
Revised: 1 June 2023
Accepted: 12 July 2023
Published: 15 July 2023

1. Introduction

Before presenting the results, it is necessary to specify the reason for the use of stainless steel resisting degradation in an aqueous nuclear environment with low-energy radionuclides. Indeed, it is crucial for an industrial process producing radionuclides that there is no radioactive leak into the environment. The challenge was addressed by examining the reliability of passive oxide on 316L stainless steel subjected to β^- radiation [1]. Therefore, this investigation is intended for scientific understanding and industrial applications similar to recycling tritiated water for nuclear fusion reactors. To do this, it is also possible to compare the energy released by the β^- source to that provided by a laser beam. Depending on the power of the laser, the oxidized layers are ionized at low energy (a few kilo-electron-volts) or decomposed at dense energy (greater than 10^4 MeV [2–4]). By this fact, the laser beam can serve as a basis to estimate the quantity of energy inducing a modification of the oxide layer. In order to study the impact of the laser beam on the oxide layers, high-power lasers have been used to examine the oxide layer, taking, for example, the surface of stainless steel. A large number of pulses introduces structural modifications and precipitations. This microstructural alteration due to the laser modifies the properties of the oxide [5–8]. In addition, the profile of the content of radionuclides bound to the oxide are higher near the oxidized outer surface, this greater content is due to its solubility and its low diffusibility. Thus, the external oxide is subjected to energy from the β^- particle, so degrading it more easily.

Therefore, this work makes it possible to estimate the state of destruction of the oxide in this environment. The β^- energy of about 6 keV per decay of radionuclide modifies the protective characteristics of oxide over a wide range of the active-passive potential determined by voltammetry. The average β^- particle trajectory is a few µm, and its displacement speed is high enough to cross the oxide thickness while the radiolytic radicals are trapped. Consequently, the β^- interacts throughout the thickness of the oxide, whereas the radiolytic radicals partially penetrate the oxidized layer considering a short scanning time. Moreover, the presence of adsorbed and ionized radicals facilitate unstable oxide

in the passivity. Consequently, the effects on the unstable oxide are questionable. This contribution will provide a detailed analysis of the passive oxide in the presence of low energy leading to chaos. In this context, characterizing chaos is a necessity.

For that, in the present paper, the approach is presented as follows:

(a) Formulation of the results obtained by voltammetry in examining the effects of β^- at the surface of steel for different impact rates (models);
(b) Formulation of the chaos data computed from the unstable oxide at the active and passive potentials for several radionuclide contents. Local chaos was clarified each time.

To broaden this topic, the method used in this study can also be adapted to the corrosion of glass (silicon oxide SiO_2) in the presence of specific radionuclides and others. After presenting the aim of this study on the unstable oxide, the results provide a correlation for the chaos technique [9,10]. This publication follows a previous one on the embrittlement of palladium cathode by hydrogen isotopes [11]. In addition, the electrolyzer is considered to contain a high concentration of radionuclides. These two publications go together, and the bibliography is common to both, and this is given in the first dealing for embrittlement. This common bibliography cites a new alloy-based Nb with enhanced hydrogen permeability, embrittlement resistance, mechanical strength, and workability [12,13]. These two studies are also supplemented by a book examining the corrosion specific to the radiolytic products formed in this low-energy environment [14]. The researchers focused mainly on irradiation-assisted stress corrosion cracking in the nuclear medium. This study aims to consider oxide stressed by low energy impacts. No essential work in the literature was reported on the propagation of stress corrosion on oxide using a chaos analyzer when low-energy radionuclides are acting, and this is why it was necessary to fill this gap. A chaos data analyzer is a research tool that allows computing numerous derivative data at constant spaced intervals. The major goal is to detect large diverging or unwanted deviations in determinism chaos. The data obtained can be displayed in phase space. The chaos data analyzer works in automatic mode, and the derivative signal is performed in full or in the local diverging sector. It is suitable for the following approach and for all low-energy radionuclides in an aqueous environment considering:

(a) energy dissipation into oxide;
(b) the unstable divergence topology when the oxide is unstable.

Concretely, four areal contents of tritiated water will be examined in this study. For these contents, the impacted oxide will be destabilized between 7×10^3 and 3.6×10^6 MeV cm^{-2} s^{-1} in this aqueous nuclear environment.

2. Experimental Equipment with Procedure for Objective

In this study, the stability of the passive oxide layer is examined using two different approaches: voltammetry and chaos data analysis. Therefore, the impacts of β^- take place in the first part of the voltammogram; then, in the second part, the chaos data are computed and analyzed.

In the first part, examined in Section 2.1, voltammetry makes it possible to carry out experimental tests of short durations, which would not have been the case by plotting the potentiodynamic curves at a low scan rate, such as 5 mV s^{-1}, where the current is free to change. For this low scanning rate, and therefore, for a longer duration of tests, the vapor pressure of water containing the radionuclide can impact safety; this is why it was chosen to work at a high scan rate in a glove-box (Figure 1). During sampling and testing, procedures were normalized to avoid accidentally spilling the radionuclide in the glove-box leading to serious contamination [15]. Another example is that spraying contaminated water in an atomic absorption spectrometry graphite crucible has to use small sample volumes (less than 100 µL).

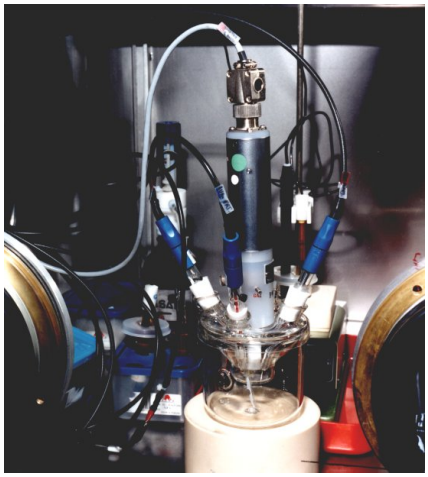

Figure 1. Electrochemical cell for corrosion tests a glove-box.

Instabilities are also easier to capture on the oscilloscope at a high scan rate. The voltammetric equipment consisted of a Radiometer bi-potentiostat and a triangular wave signal generator (PRT 20-2 and GSTP 3) connected to a Tektronix 2230 digital oscilloscope. To avoid using too large a volume of tritiated water, the size of the double-walled electrolysis cell was as small as possible; consequently, the surface of the electrode was appropriate. The cyclic voltammograms were drawn by a Hewlett-Packard HP 7440 AXY plotter. The working electrode was a rotating disk-ring electrode. The disk of 0.1 cm^2 surface consisted of a 316L stainless steel rod of commercial availability. An ultramicroelectrode for even smaller surfaces exists for particular needs, not for us. The working surface was perpendicular to the axis of rotation to avoid turbulent flow. The 316L stainless steel was firmly inserted into a Teflon holder in order to avoid electrolyte infiltration at the stainless steel/holder interface, which often causes random errors in the data. Therefore, special care was taken to manufacture an electrode suitable for noise measurements. The rotating electrode induced convection phenomena within the electrolyte. In contact with the surface, an area of electrolytes was immobile, called the boundary layer. Its thickness was very low (1 to 10 µm). The amount of radionuclides was very low in the boundary layer. Its concentration considered must be constant during the measurement to avoid radionuclide depletion in the boundary layer and the need to work with a small surface and a controlled supply of radionuclides by convection is necessary. Prior to each use, the disk electrode was mechanically polished using 2000 mesh-grade silicon carbide sheets and washed with deionized water. In these conditions, the roughness factor for stainless steel measured using a profilometer was estimated to be 1.3. A saturated calomel electrode (SCE) and a platinum electrode were used as reference and counter electrodes. To avoid capacitive and inductive interferences, a platinum wire was added to the reference electrode with a 0.1 pF capacitance. The voltammograms were scanned cyclically at a sweep rate of 200 mV s^{-1} from the lower cathode potentials, into the prepassivity, the passivity, and up to the transpassivity by successively increasing the radionuclide content. The noise was examined until reproducible graphs. The equipment and the experimental scheme for taking reliable samples from the confined enclosures were as follows:

- A reinforced glass safety small jar;
- A puncturable flexible membrane placed at the opening of the jar;
- A syringe allowing the perforation;
- A sampling head to guide the syringe in order to protect the operator's fingers.

During sampling, the jar was in depression. Along with the corrosion tests, microanalyzes were performed to look for radiolytic anions and cations specific to this medium.

In the second part, examined in Section 2.2, electrochemical noise was extracted from the UnScanIt calculator. UnScanIt is useful for digitizing a sequence of points that cannot be controlled by any other digitizing method. It assigns the exact location in coordinates

for each point location, and the point can be used to assess the accuracy of that particular point assignment before using the chaos data analyzer. The data obtained were computed in the chaos analyzer for detailed arrangements. The chaos data analyzer is a collection of 14 programs that allow analyzing a record of up to 16,000 data points representing quantity measured at equally spaced intervals. If the intervals are the time, the method is referred to as time-series analysis and the record is a typical signal displayed on a screen. The major goal of a chaos data analyzer is to detect hidden determinism chaos in seemingly random data. When chaos is found, tools are provided to enable the prediction of properties for the next values in the time series. The program is used as a research tool for non-linear dynamics. It is written to move from one analyzed sequence to the next. It has an automatic mode in which all the tests are performed and the results are provided. The program gives a wide variety of information useful in analyzing potentially chaotic data. It provides a collection of chaos-oriented analytical tools. The extra pieces of information are the data manipulation, the graph of data, the Lyapunov exponent, the correlation function, the correlation matrix, and the phase space plots. The ability to create your own input data is a very useful feature. The analysis includes a search for structure in the phase space plots. High-order derivatives can be plotted as well by successively differentiating in the data manipulation program. During the reconstruction of the attractors, a correlation function is used by the chaos data analyzer to determine how random the data are. This enables acquiring the dependence of unstable oxide on the applied potential and the density of impacts of β^- energy. In these sequences, the chaos data analyzer detects the singular deviations (events) for the computed data [16]. In the 2D or 3D mesh format, the projection of the determinism represents the phase space depending on the contribution of the operatory conditions. A non-random number of iterations of 5-ms is imposed on the time, or on the potential, making it possible to visualize the chaos relating to the unstable oxide layer. The acquisition of frequency and signal data was carried out by sweeping from the Flade potential to the transpassivity with a step of 0.2 s, which represents a good number of passes to explore, i.e., a hundred time series. For the sake of simplicity, we selected only the most significant key outcomes, eliminating duplicate repetitions; otherwise, this article would be invaded by an unexplorable local phase space given their number. Chaos data analysis provides data on the integrity of modified oxide structure leading to stressed oxide morphology and a destabilized oxide state. When entanglement is present, calculation provides the Lyapunov exponent and divergence enabling the determination of qualitative characteristics of the oxide. The chaos analyzer can work using small sectors to predict a singular local event. In these tests, the phase space portrait makes it possible to visualize the chaos and the organization of oxide. Finally, the sample was examined with a Jeol scanning electron microscope to observe corrosion and stressed oxide problems. The schematic of the experimental setup can be summarized as follows:

- Surface preparation of 316L stainless steel;
- Draw the voltammetric curves;
- Use the oscilloscope data;
- Check values using UnScanIt;
- Perform these values using the chaos data analyzer.

2.1. Electrochemical Aspects

Voltammograms were obtained on 316L stainless steel at a high sweep rate in active and passive potential. Operatory conditions: surface area: 0.1 cm^2, NaOH: 1 mol dm^{-3}, scan rate: 200 mV s^{-1}, ω: 2000 rpm, cathodic scan limit: −1.75 V/SCE, anodic scan limit: 1.00 V/SCE.

The characteristics of oxide are as follows in the voltammograms:

(A) active peak A;
(B) Flade event B;
(C) passivity C;
(D) transpassive peak D;

(E) transpassivity E;

Voltammetry is a powerful tool for exploring instability. The curves in Figures 2–5 were constructed using a low-energy radionuclide at different contents impacting the stainless steel surface. The density of the energetic impacts on the oxidized surface is given in these graphs. These curves were started in the anodic scan to examine the characteristic events. The lower cathodic potential limit for scanning corresponds to hydrogen evolution. Scanning the potential leads to the active peak and the Flade event (−0.35 V in Figure 2), corresponding to the transitory formation and rearrangement of the micro-structure of oxide during β^- sorption [14]. Facing chaos, it is necessary to limit the route to analyze the unstable events between the active peak and the transpassive potential for the stressed oxide. Effectively, one of the aims of plotting these diagrams was to interpret the β^- effect. Based on the interpretation, an electrical scheme is given to obtain the various instabilities. This involves chaos, where the oxide layer and energy affect the stress.

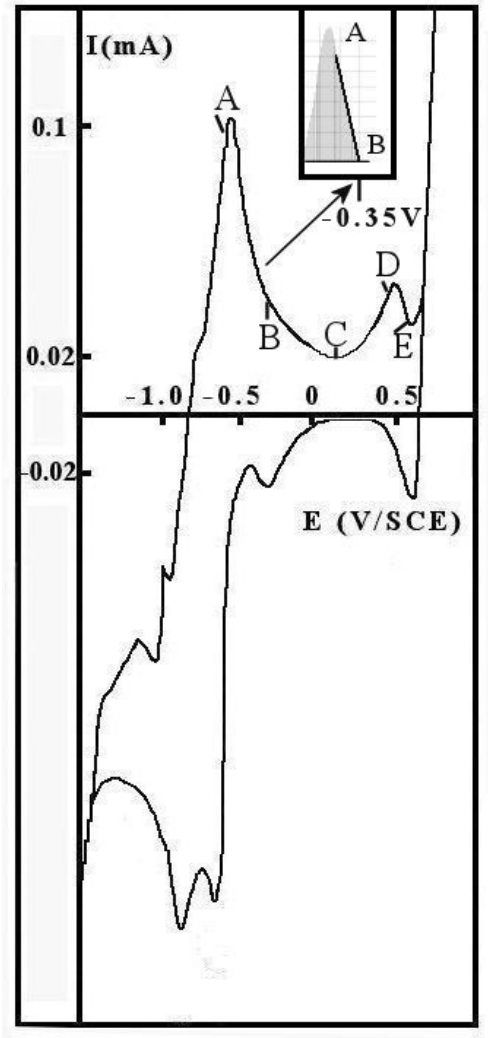

Figure 2. Voltammetry, Model 1, 1.2 × 10^6 β^- impacts cm^{-2} s^{-1}, Window: determination of Flade potential by PeakFit program.

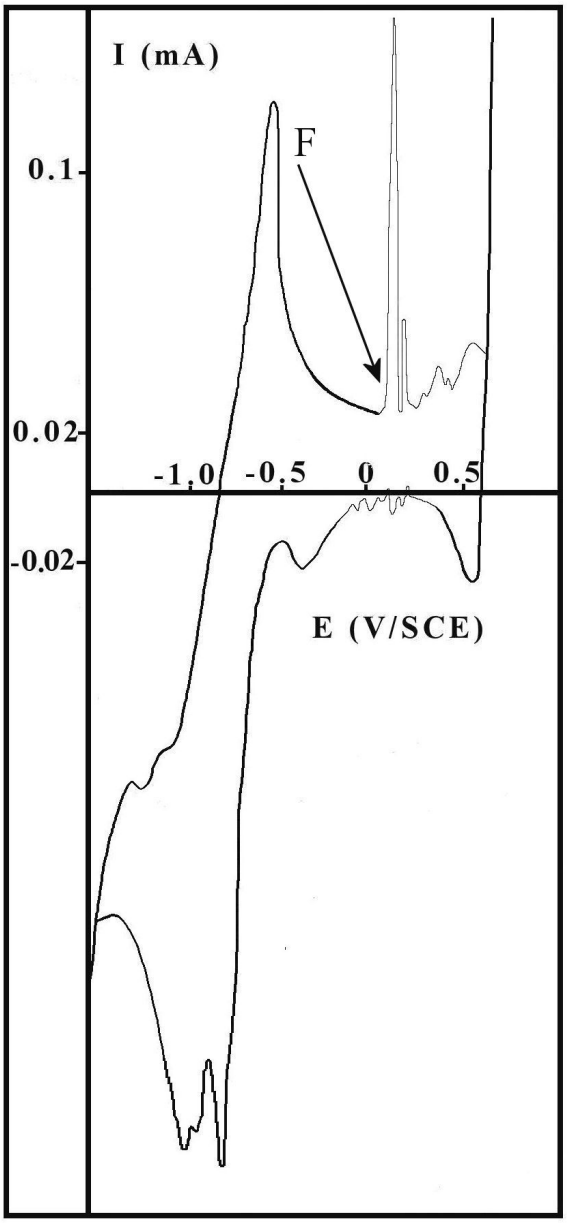

Figure 3. Voltammetry, Model 2, 6×10^6 β^- impacts cm^{-2} s^{-1}. Array: instability in pseudo-passivity.

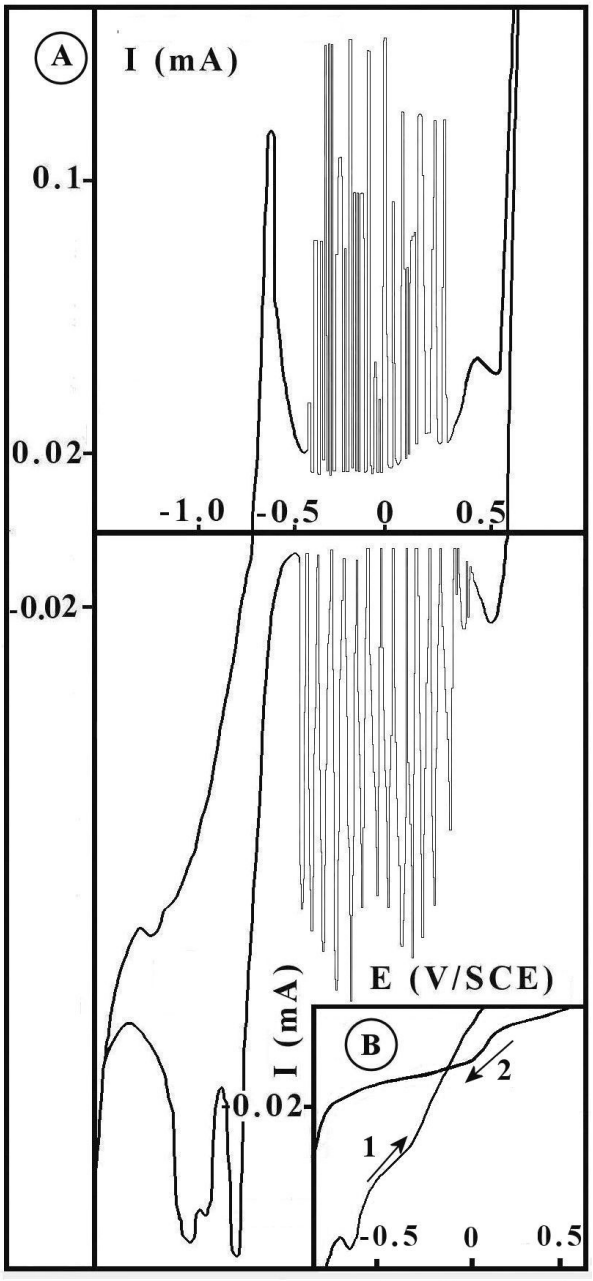

Figure 4. Voltammetry, Model 3, A: disk, B: ring, 6×10^7 β^- impacts cm^{-2} s^{-1}.

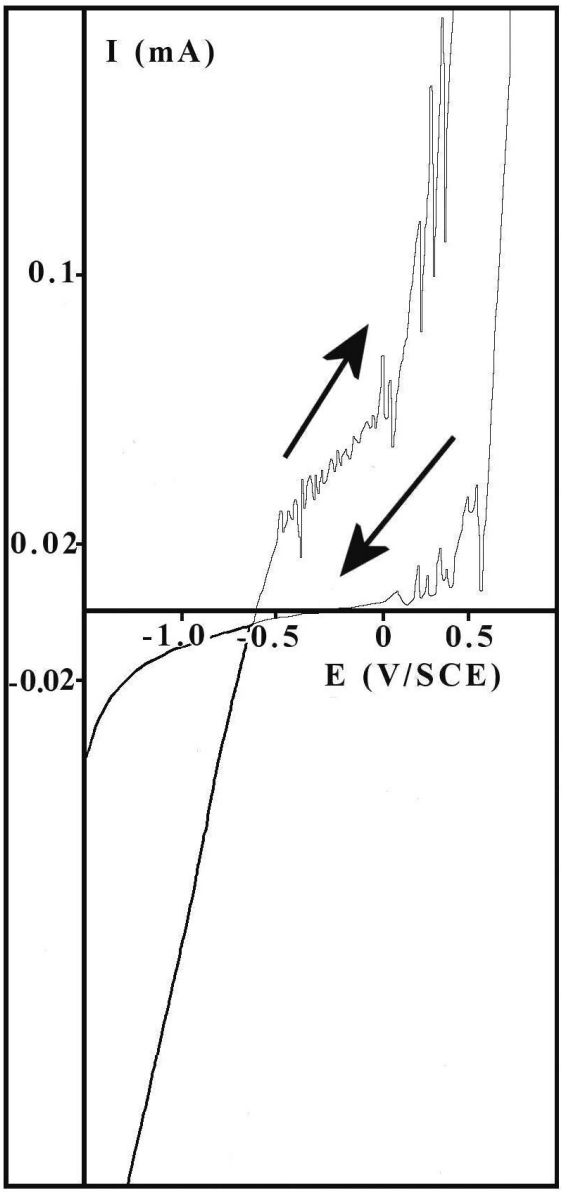

Figure 5. Voltammetry, Model 4, 6×10^8 β^- impacts cm^{-2} s^{-1}.

In Figure 2, instabilities are questionable for low scattered impacts of radionuclides, whereas Figure 3, obtained at medium impacts, shows a few instabilities (F). Considering the hydrated oxidized layer covered by low-energy radionuclides releasing destructive energy onto oxide, the charge is enough to destroy oxide by the impact of the β^- particle. In Figure 4, part A, the instabilities are abundant for this superficial energy. These figures show that the Flade potential is near the active peak and the passivity is acting for oxidation of stainless steel. This means oxidation in the presence of the β^- particle is possible with localized stress corrosion. Local oxide stress also involves destabilization with activated OH^* hydroxide and HO_2^* peroxide radicals. Examining Figure 4, part B, the cathodic current obtained in the forward (1) and backward (2) scans on the ring corresponds to the electrochemical reduction in the corrosion products formed from the disk. This current is not negligible and means the destruction of the passive pseudo-layer during instabilities. These intertwining phenomena explain how stress corrosion can be produced on 316L stainless steel by β^- energy. It should be noted in Figure 5 that there is no prominent active peak but a regularly positive increasing current for this critical β^- energy impacted at the surface. This signifies no existing protective oxide, and the alloy is largely exposed

to this aggressive medium. The electrochemical process suggests that β^- is expected to diffuse in the ionic lattice of oxide via activation; for example, by OH^*, then blocked diffusion occurs in contact with the alloy. Moreover, the activated oxide layer ceases when all oxide is eliminated in the transpassivity and before. Noise is possible in oxide with the combination of OH^* and β^- particles. The surface is easily over-covered by the radiolytic hydroxide oxide. To access valuable information on the β^- charge into oxide and the stress corrosion highlighted by the noise, results were examined from the equivalent electrochemical circuit model given in Figure 6 ([17–21]). Our goal was to apply it with the elementary linear electrochemical elements for the stable oxide (part a): resistor, capacitor, and complex impedance. In part (b), the oxide memristor is based upon the O^{2-} vacancies as a positive or negative variable [4]. The hysteretic behavior of the memristor gives rise to the characteristic double-loop. The double-loop of the memristor is entirely different from the other basic elements of the circuit: resistor, capacitor, or inductor, and it is difficult to analyze the impedance by electrochemical impedance spectrometry. Interesting results on impedance spectroscopy and oxide-based memristive devices can be found in detail in [22]. It provides an implementation of chaos based on a non-linear active Chua model. The concept behind this implementation will integrate the β^- striking oxide giving the characteristic of noise [23]. The electrochemical noise will put in evidence the stress corrosion of oxide when the non-linear element is detected. Therefore, when using a chaos analyzer, scrolls and loops are identified as events regarding the stable spectra. The active system has periodic or aperiodic orbits or loops over a specific range of parameters. In exploring the core in orbit, the oxide should be reactive; whereas, alternately, the "eye" is neutral. Therefore, we will study the core in perfect harmony with the results obtained in voltammetry. In the case of oxide non-perturbed, the core, nominally stable, will present a trajectory of the Lissajous type. A qualitative change should be noted when the dynamic parameters vary. This involves a difference in stability with the modification or destruction of one or several orbits, coalescence, or annihilation depending on the aspect of oxide destruction [24]. Looking at large diverging or unwanted deviations due to β^- charging, there are few detailed models of chaos in the corrosion literature [25,26]. For this reason, this work focuses on the description of this concept.

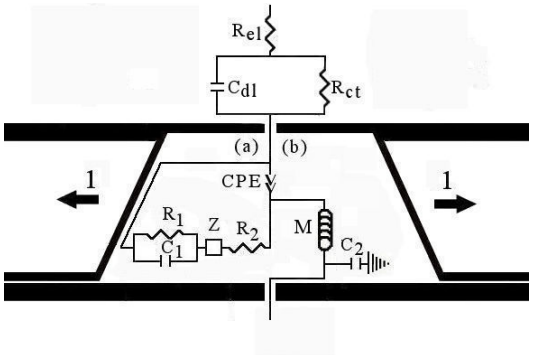

Figure 6. Equivalent electrical circuit for the behavior of oxide in contact with β^- particle. R_{el}: electrolyte resistance, R_{ct}: charge transfer resistance, C_{dl}: double-layer capacitance, $R_{1,2}$: oxide charge resistance, $C_{1,2}$: oxide charge capacitance, CPE: pseudo-constant phase element, Z: complex penetration impedance into oxide, M: variable oxide memristance, 1: β^- diffusion into oxide, a: complex part, b: unstable part.

The results of chaos should agree with the electrochemical noise. The complex dynamic depends on the insertion of the β^- particle. From this perspective, the stress in depth corresponds to several tenths of a nanometer in oxide. This corresponds to the penetration of the particles in the oxide. High stress can induce compressive oxide. The complex dynamic should show the effects of β^- particles on the derivative. The distribution varies in the oxide, so the β^- particle plays an unpredictable role in it. This results from an increase or decrease in β^- particle penetration inducing stress before destruction. According to the

modification of oxide, it is somewhat elusive to conclude the voltammetry curves. This is why we have looked at the spectra obtained by the chaos technique.

2.2. Chaos Analysis and Result Projection

The high scan amplifies the micro instabilities obtained on the voltammograms. These are correlated with the chaos analyzer by acquiring the data and differentiating the derivatives. To comprehend the chaotic events produced by the β^- transfer into oxide, the path of the raw data has to be examined as in [11]. The investigation concerns the variation of the derivatives between the $\partial i/\partial E$ and the time, which enables estimating the oxide breakdown. In this case, implanted energy, potential, and time play essential roles in chaos. Effectively, the phase space helps to interpret events in the oxide layer subjected to β^- particles. From the global spectra, the concerned impacts examined are in Sections 3.1, 4.1, 5.1, and 6.1.

3. Model 1, Measurements for 1.2×10^6 Energetic Impacts cm^{-2} s^{-1}

3.1. Aspects of Global Spectra

The destruction of the passive oxide layer is highlighted by the dynamic impacts of incoming β^-. An attack expanding in the subsurface is progressively produced regarding instabilities (Figure 7). In this Figure, the X-axis represents the time when the potential is scanning. The Y-axis is the relationship between the first derivative of the current (∂i) and the iterated potential (∂E). The temporal frequency of instabilities in this figure is the number of similar and repetitive pulses per unit of time. It is possible to analyze them for more clarity and to distinguish the different spatial events. The frequency measured for the major impacts is between 0.6 and 1.2 events per second.

In this graph, the Flade potential is represented by event 1. In contrast, the major part corresponding to pseudo-passivity is scaled for 10^6 (event 2), and the part corresponding to transpassivity (Figure 2 E) is scaled for -5×10^6 (negative event 3). The β^- transfer and oxide destruction can be modeled from the complex chaos loops and rated to the impact density for the pseudo-passive potential on the full or local spectra (Figure 8). Figure 8 illustrates the aspect of discernible structure in the perspective drawing. The "eye" corresponds to a very dense collection of data showing the compactness of event 1. It is associated with the nucleation loops after the transition from the unstable to the stable state or vice versa, these modify the structural properties of the oxide. The pseudo-passivity loops are not dense (event 2), meaning that the attack is not severe for this impact density.

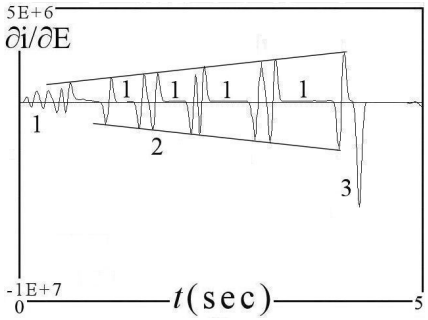

Figure 7. Instability events in the full range of potential for 5-s, 1: in the Flade potential, 2: in the pseudo-passivity, 3: in the transpassivity.

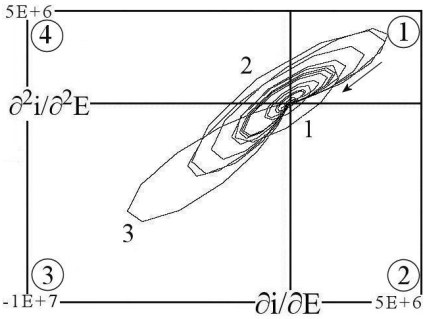

Figure 8. Phase-space derivatives, 1: in the Flade potential, 2: in the pseudo-passivity, and 3: in the transpassivity.

The loops can be correctly analyzed in the phase space plot by selecting a suitable time duration in the dynamic core and deviation as in the following local examples. Consequently, the converging point in the core (event 1) depends on the weak density of β^- impacts in the Flade potential limiting stress. Modification of the oxide structure by β^- indicates that high impacts will lead to a stressed morphology, not guaranteeing a good performance of pseudo-passive oxide (event 2). This shows that the β^- particle is not limitative in-depth. It behaves like a particular impedance, where the β^- particle penetrates oxide (Figure 6). Considering a protected passive oxide layer, protection is effective for tens of nanometer depth. Therefore, the spectra make it possible to predict when the oxide morphology is modified with the production of defects from the internal β^- flow in depth. According to the analyzer, the local phase space has positive Lyapunov exponents characterizing the chaotic impacted state in the pseudo-passive potential for 1.6, 2.2, and 2.9-s (event 2). For the decreasing activity, all Lyapunov exponents are negative in the local prepassive zone of phase space. A stable state can be obtained when the exponent is near zero, but a bifurcation is possible in the unstable state. The phase space of positive or negative variation indicates that the energy flow will not be uniform, temporarily not stable to be chaotic, and will depend on the impacted flow.

3.2. Aspects of Local Sectors in Spectra

The irregular part of the orbit should make it possible to identify the propagating stress. In this connection, the trajectory has to be considered for β^- penetration into oxide [27,28]. The activated oxide represents the front profile of loops, including different possibilities for the active energy produced by the β^- decay particles into oxide. It is possible to apply the electrochemical model sharing its parameters with the β^- energy into a template for dynamic potency (Figure 6).

If the phase space derivative variation leaves the core or diverges in the first quarter, the system will become unstable. On the contrary, the system is stable if phase space goes in the "eye" or the third quarter. Concerning the second and fourth quarters, the system is variable for going in the first or third quarters. In A and B of Figure 9, the loop in prepassive potential (event 1) indicates some erratic instabilities not significant of breakdown oxide. Conversely, in Figure 10, event 2 indicates the premise of oxide modification before pseudo-passivity (event 3). In Figure 11, perturbed events 1 and 2, the system is pseudo-stable with two small split loops around the "eye". The loops do not reveal much, and the impacts are few. The depth penetration must be limited. There are β^- different penetrations in the oxide layer depending on the active or pseudo-passive potentials and the morphology of the oxide. When varying a parameter, quasi-stable chaotic routes are expected. Under the appropriate condition, chaos can present loops corresponding to the density of β^- energy in a pseudo-stable or unstable state over a potential picked in Figures 9–11. Their distribution thereby produces various $\partial i/\partial E$ derivatives in the function of time (B in Figure 11). The Lyapunov exponent of the derivative cannot always be negative or near zero on the trajectory, but it can give the variable trend. At first, there is the Flade potential where hydrated oxide is not stabilized, then the pseudo-passivity, and the remaining is at

the end of pseudo-passivity. At this stage, the graphs demonstrate the feasibility of analysis for the β^- adsorption-penetration with chaos for appropriate potentials.

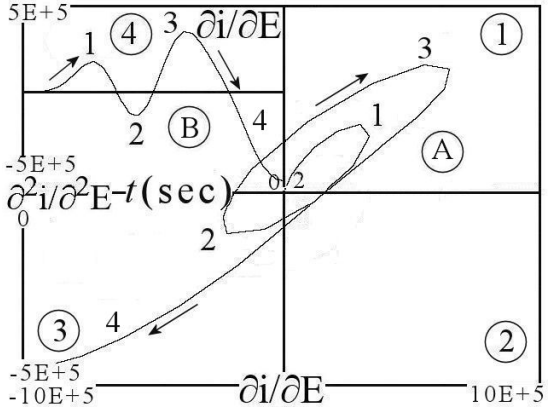

Figure 9. Diverging sector, 0.2-s passed the Flade potential and for the 0.2-s duration, 1: in the local core, 2: in the loop, Lyapunov exponent: 0.329 ± 0.334.

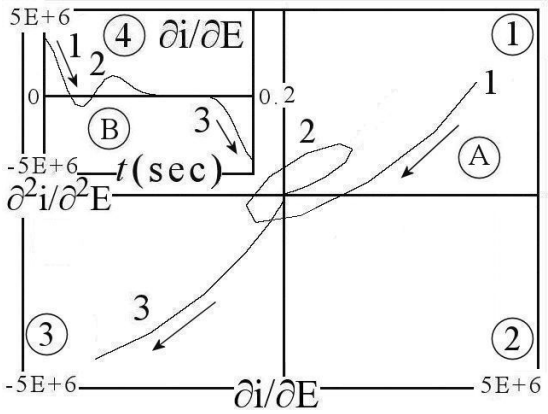

Figure 10. Diverging sector in the pseudo-passivity, 1.6-s passed the Flade potential and for the 0.2-s duration, 1: in the loop, 2: in the deviation, Lyapunov exponent: 0.195 ± 0.347.

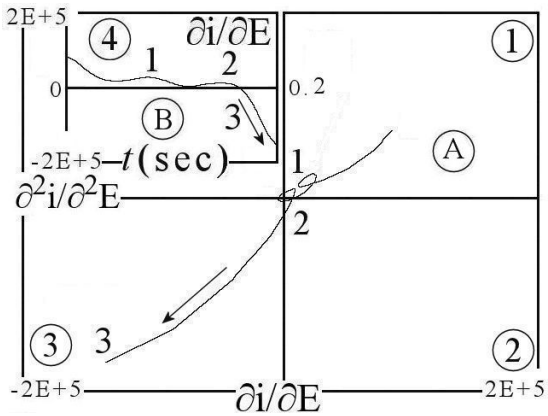

Figure 11. Diverging sector in the core between the last pulse in pseudo-passivity and the pulse in transpassivity, 3.7-s passed the Flade potential and for the 0.2-s duration, 1, 2: double small loops in the local core, 3: in the deviation, Lyapunov exponent: 0.627 ± 0.347.

4. Model 2, Measurements for 6×10^6 Energetic Impacts cm^{-2} s^{-1}

4.1. Aspects of Global Spectra

Figure 12 shows unstable denser and higher pulses in charging energy of 3.6×10^4 MeV cm^{-2} s^{-1} β^- particle onto oxide. The frequency measured for the major impacts is 0.7 events per second, this does not increase with the impacts. In this figure, the horizontal line near zero is a consequence of pseudo-stability in the "eye" (event 1). At low potential for the 0.5-s exposition of β^- energy, the derivative depends on oxide organization in the active potential (event 2). The derivative makes it possible to differentiate short-lived events.

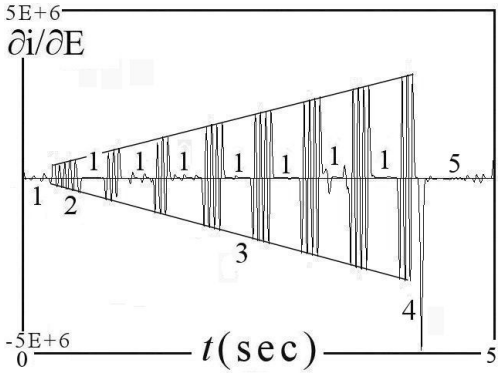

Figure 12. Instability events in the full range of potential, 1: in active peak, 2: in the Flade potential, 3: in the pseudo-passivity, 4, 5: in the transpassivity.

This derivative is a response to the unstable oxide on the active or pseudo-passive potential. The graphs in Figures 12–15 in 2D or 3D dimensions depict four positive and negative derivative signals:

(a) Centralized points indicating steady-stable in pseudo-prepassivity (event 1);
(b) Minor positive and negative instabilities in the Flade potential (event 2);
(c) Significant instability scaled highly positive signal synchronized with highly negative signal in pseudo-passivity (event 3);
(d) High negative signal synchronized with the unstable event in transpassivity (event 4).

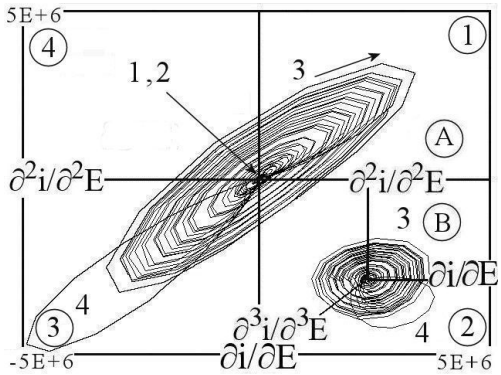

Figure 13. 2D and 3D views of phase space derivatives in all pseudo-passivity for 5-s from the Flade potential, time in passivity: 4.5-s, and time in the transpassivity of 0.5-s.

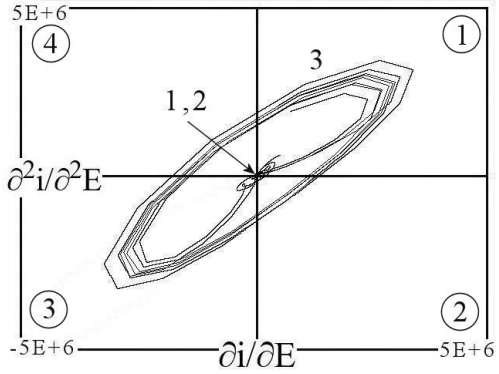

Figure 14. Phase-space derivatives in the pseudo-passivity, 3.1-s passed the Flade potential, extended to 1.4-s.

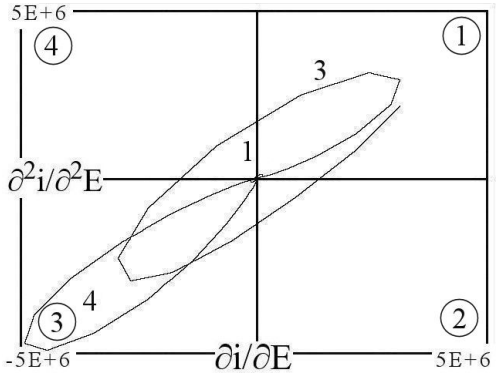

Figure 15. Phase-space derivatives in the transpassivity, 4.5-s passed the Flade potential, extended to 0.5-s.

The detailed Figures 14 and 15 describe partial large sectors with high and tight scrolls in the derivative data for pseudo-passivity and transpassivity. Higher positive scrolls in the first quarter do not pass by the origin of axes corresponding to the oxide-breaking state (event 3). At the same time, the scrolls in the third quarter and the centralized signals signify organized complex oxide where protection is possible (events 1–2). The scrolls passing or not through the origin of the axes signifies the variability of the system. It is possible to visualize the time of instability or stability in Figure 12 for pseudo-passivity. The last negative pulse corresponds to the pseudo-oxide activated by β^- energy in the transpassive potential (Figure 15 event 4).

Figures 12 and 14 show that the low value near the "eye" between two serial pulses corresponds to a pseudo-stationary state. During fast events occurring at large energy, free electrons from β^- particles moving into oxide are intense, thus favoring charge transport and oxide ionization (O^{2-}). Alternatively, when minor events are present, filtering oxide acts and insufficient energy accumulates in all oxide thicknesses for breakdown. The state is pseudo-stable. If there is nothing to slow down energy, all the energy is released into the oxide, followed by a non-stationary state. Therefore, the regime can be non-stationary, depending on the dense energy. For a good interpretation, many small partial images are necessary to interpret the chaos correctly.

4.2. Aspects of Local Sectors in Spectra

The increase in pseudo-passivity potential theoretically affects oxide growth, and the chaotic loops change with larger periodic sequences, indicating growth and stress in the oxide. There is a predictable orientation in the spectra. The loops appear one after the other in the first or in the third quarter transiting by the temporary second and fourth quarters. Regarding the instability events shared with the loops, oxide destruction globally occurs on

the base of ionized adsorbates by the energetic β^-. Consequently, electrochemical stress is due to a sufficient amount of ionizing energy degrading oxide in the juxtaposed episodes.

To know how time acts, analyzing small spectra sectors is necessary. The chaos can be dynamically complex, consisting of one or more events in the phase space portrait. These can be decomposed into sectors of several sizes. The Chua circuit can be incorporated into the complex oxide ionized by the β^-. The medium impact influences the chaos induced by more impacted β^- energy. Therefore, in this concept, corresponding to oxide excited in deep, chaos implies that raw data vary. This dynamic chaos system is characterized by a dense collection of periodic or aperiodic pulses (Figure 12 event 3) or scrolls sensitive to the implied energy in the raw data (Figure 13) so that events can evolve quickly into different aspects. However, chaos should be in a deterministic evolution despite an irregular appearance (event 3). In addition, it can be seen that no periodic event may survive in the boundary data after sufficiently strong perturbation in the chaotic system in a local sector. This is mainly where the periodic events $\partial^2 i/\partial^2 E$ fall in the "eye" signifying possible temporary no action onto oxide before going to the next sector.

From Figure 14 events 1–2, the chaos spectra for the pseudo-prepassive oxide passed the Flade potential show small loops (Figure 16 scroll 2). The excited OH* into pre-oxide corresponds to adsorption with diffusion and diffusion of β^- energy in its depth. The diffusion of OH* is slower than that of the β^- particle. In this figure, the small loops appear for a gap of 0.2-s (scroll 2). From scrolls 1–2, it is suggested that the β^- distribution is not locally uniform, depending on the trajectory and local decay, and activation is produced with partial coverage in any direction. This model combines adsorption-transfer charge. Absorption and diffusion of OH* appear in the electrical circuit. The studied local sector can be linked to the perturbed transport and should describe the perturbation in time (0.2-s each) for finite depth while forming different short neighbor scrolls (events 1–2) in Figure 16.

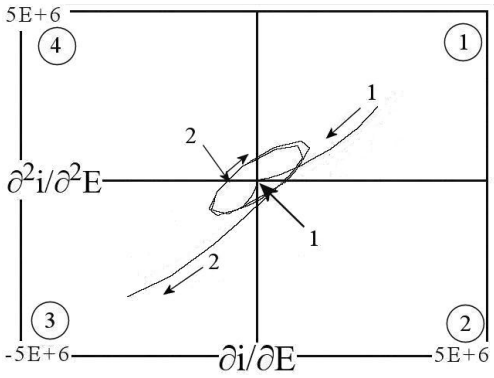

Figure 16. Comparison between two local sectors (1, 2) in the pseudo-prepassivity. Converging sector 1: 1.0-s passed the Flade potential, Lyapunov exponents: 0.374 ± 0.863. Diverging sector 2: 1.2-s passed the Flade potential, Lyapunov exponents: 0.168 ± 0.378. For 0.2-s duration each.

These fast events show the complex evolution of this system where β^- energy is acting. The event becomes less observable if energy is too low or not penetrating enough (scroll 1). The reverse behavior arises when the penetrating energy amount is high (scroll 2). Furthermore, neighboring values for the characteristics can lead to coalescence in the core (Figure 16, scrolls 1–2). It should also be noted that the Lyapunov exponent corresponding to the scrolls is stable in sector 1, seen in Figure 17, and moves to the higher cycling values in sector 2 when its amplitude increases, signifying that stress is increasing into oxide depth. Erratic loops passing by the origin of axes in the pseudo-prepassive potential indicate oxide modification not impacting stability. Indeed, the instabilities are not visible on the voltammetry curves. Some repulsors can work with an angular loop when examining the trajectory by the third derivative $\partial^3 i/\partial^3 E$ in equatorial projection (Figure 17 sector B).

Comparison for the core in sector B can be made with sector A-2 confirming the same aspect in the pseudo-passivity.

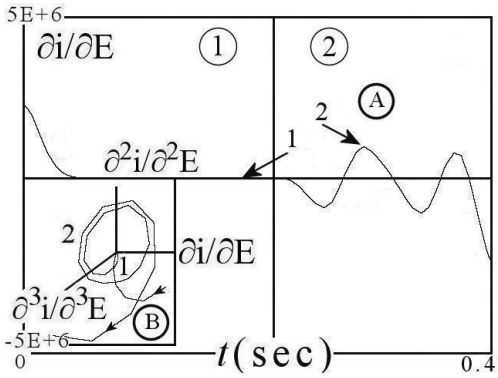

Figure 17. Derivative in the function of time (A) and diverging sector in 3D dimensions (B), in the pseudo-prepassivity, 1: 1.0-s passed the Flade potential, 2: 1.2-s passed the Flade potential. For 0.2-s duration each. Lyapunov exponents: 0.515 ± 0.246. According to Figure 16 scrolls 1, 2.

Figure 18 scroll 1 looks like Figure 16 scroll 2, except that the loop does not pass through the origin of the axes ("eye"), meaning a more intense interaction with the β^- particle. In this, the chaos diagram subjected to the pseudo-passivity shows the respective events depending on adsorption and diffusion at these potentials. Fast event 1 confirms the hypothesis that adsorbed β^- penetrates oxide for a short time before fast diffusion and blocking diffusion when it arrives at the metal. The loop in the core provides a value near zero related to changing transfer characteristics. It corroborates an interaction on the oxide layer, unlike the position in the "eye" where there is no action. In this case, the electrical schema (Figure 6) generates various paths for the β^- particle. This model can be retained for diffusion into oxide by the β^- particle in the pseudo-passivity. If enough particles are used for diffusion, these act to modify oxide. The energetic electron diffusion corroborates absorption in the entry surface. The effect affects the characteristic of oxide. According to the content of β^- for these specific pseudo-passive potentials, the oxide layer cannot be considered a strong barrier against corrosion passed the Flade potential.

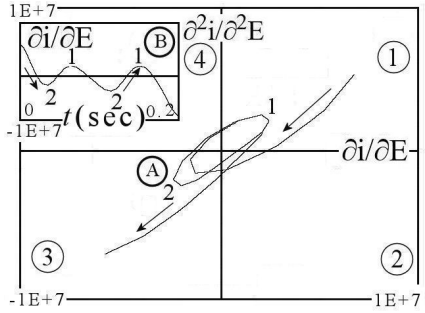

Figure 18. Diverging sector, in the pseudo-passivity, 3.6-s passed the Flade potential for the 0.2-s duration, Lyapunov exponent: 0.156 ± 0.301.

To better discern the instabilities in event F in Figure 3, we extracted data on chaos in this zone from Figure 19. In sector A, the numerous loops in the core (event 1) correspond to unstable oxide, as seen in sectors B and C in the function of time. Micro-event 2 corresponds to pseudo-stability in the "eye" in A and the perturbed horizontal line after decreasing instabilities in B. The matrix correlation in C is entirely obtained in the positive first quarter signifying unstable events in 1, as predicted in Figure 3.

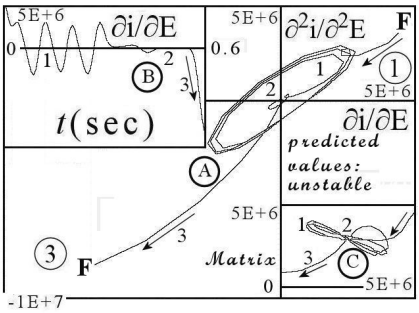

Figure 19. A: divergence sector, B: derivative in the function of time, C: correlation matrix, 4.2-s passed the Flade potential, for the 0.6-s duration, according to Figure 3, in the sector of F. Lyapunov exponent: 0.414 ± 0.232.

According to these results in Figure 19, we locally detailed the potential of event F in Figure 20. For that, the trajectory of the third derivative in C shows emerging scrolls in the first quarter and an unstable matrix. Such behavior not passing through the origin of the axes follows divergence in event 1. Once the oxide is disturbed, positive derivatives (event 4) appear along the equatorial axes of $\partial^{2,3}i/\partial^{2,3}E$ (sector C and enlarged sector D). These correspond to the reorganization of oxide. The interconnection is possible between the energetic electrons and the compressive dynamic of oxide, which is no longer stable at these potentials. This reinforces the idea that the phase space derivatives are fruitful in revealing the complex level of instability. This is pertinent to the variability of Lyapunov exponents. Scrolls are related to the dynamic of morphology in oxide. According to these derivatives, the proposed chaotic system is a reliable system with difficult interpretation.

The characteristics of chaotic events in the phase space derivative depend on the potential and time. For that, analysis has to play a crucial role in representing the significant spectra to understand the property of a stationary and non-stationary signal [29,30]. However, it cannot be easy to interpret them, and they must be appropriately evaluated. The main problem is that the evolution of the signal must be followed and divided into sectors when using the chaos function to discern the different events. Therefore, analysis has to locate these events not visible in large spectra. These should show the consequence of significant energy where instability is produced and acting onto oxide. To save time, extraction of the signal should be limited to the most important parts of the phase space. The signal must denote the characteristics of the dynamic and chaotic system. A misshapen characteristic as significant instability on the pseudo-passivity corresponds to impacts formed on the oxide surface. Moreover, the matrix can be challenging because it is nearly associated with the β^- impacts. In this condition, oxide should be destroyed through this context. The electrochemical chaos analyzer provides a criterion of stability or instability for oxide. The chaos becomes visible for an energy source of 6 keV and 6×10^6 impacts cm^{-2} s^{-1}.

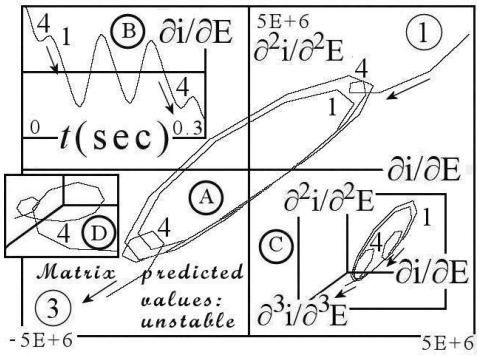

Figure 20. Diverging sector, in the pseudo-passivity, 4.2-s passed the Flade potential, extended to 0.3-s. According to Figure 19. Lyapunov exponent: 0.335 ± 0.219.

As soon as β^- impacts are produced, the singular loop indicates how oxide is affected. The β^- particle gradually affects the oxide reaching modification of the structure. From the spectra, it is seen that the Lyapunov exponent in the core is variable, thus assessing the level of chaos. In this case, the chaos level signifies a substantial change in the amount of β^- accumulated in the oxide subsurface. This suggests its presence in depth. An increase in diffusion indicates less structural compactness of the oxide. The Lyapunov exponent shifting to a higher positive value signifies increasing the deep of β^- penetration into oxide. But, if the values spiral along the "eye", the system becomes stable. This is experimentally established for this structure as it corresponds to a typical stable oxide. Pseudo-stability is obtained, reflecting better oxide properties. Then, it forms a uniform trajectory in the third quarter to present a Chua circuit for a semblance of stable behavior. As a deduction, the spectra are dominated by unstable events occurring when oxide nucleates and propagates.

Regarding the perturbed events, 5 to 7 in the enlarged Figure 21, obtained at the end of the event F from Figure 19 event 2, a meta-stable scroll passing through the "eye" is formed where the β^- particle impacts the kinetic of chaos. If the signal remains stable in the "eye", either the chaos disappears, or it slowly progresses into oxide. The signal may indicate pseudo-passivity followed by stabilization (event 7). It can be coupled with propagating stress in-depth or small negative evolution (events 5–6). The stress corresponds to a steadily increasing instability by the β^- energy during the growing impacts. Instability in Figure 19 falls when $\partial i/\partial E$ becomes very low in the "eye" (Figure 21 events 5–7). Undeniably, the tendency leading to a low value in derivative gives rise to regular decreasing stress. In Figure 14, integrating the positive and negative loops shows that these are oriented sequentially around the "eye", signifying that events cannot be dissociated. Moreover, a negative oscillation can be produced after previous low instability, oscillation corresponds to the pseudo-passive potential. The results correspond to the variability of the Lyapunov exponent. These events are hardly detectable by voltammetry or large phase portrait, but this method is useful for understanding. Figure 22, obtained at the end of pseudo-passivity, shows ellipsoids shaped as a resonant event for a small time-lapse. Intermittent pair ellipsoids are produced sequentially, passing in the "eye" (events 2, 3). These illustrate the continual nucleation of oxide transformation followed by its possible catering in the small perturbations of the derivative in section B. They correspond to a stable behavior and energetic restructuring in the pseudo-passive oxide. The perturbations depend on the potential and impacted energy. Regarding the size of these events, oxide should thicken and limit the stress despite the amount of impacted energy. The breaking point of these events is visible around the origin of axes. This signifies impacted oxide. Spectra can be interpreted as competitive phenomena for oxide and diffusion near the equilibrium "eye".

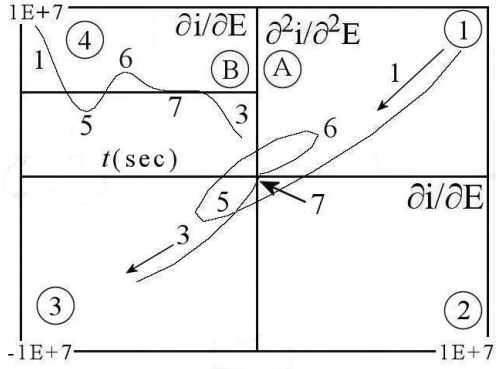

Figure 21. Diverging sector, in the pseudo-passivity, 4.4-s passed the Flade potential, for the 0.2-s duration. According to Figure 19. Lyapunov exponent: 0.225 ± 0.165.

Let us go back to Figure 22 event 4, the trajectory forms a negative lone spiral turning on itself along the final trajectory in the third quarter. The rolling up and spiral correspond to attractive rearrangement and represent stable oxide. The system can be called pseudo-

bounded because a negative Lyapunov exponent is close to the equilibrium point (−0.002 in Figure 22).

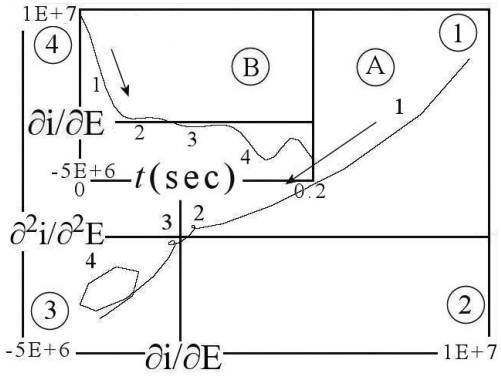

Figure 22. Diverging sector, in the end of pseudo-passivity, 4.8-s passed the Flade potential, for the 0.2-s duration, Lyapunov exponent: -0.002 ± 0.256.

The photograph in Figure 23 obtained by Scanning Electron Microscopy shows numerous oxide bursts. These are obtained at 0.15 V/SCE (Figure 3 event F, and Figure 19) in the pseudo-passivity. Therefore, it is essential to note that bursts depend on β^- particle density and potential. They corroborate the presence of the destroyed oxide lattice in the subsurface. In deduction of microscopy examination, pseudo-passivity drops in the presence of the β^- diffusion, leading to oxide breakdown.

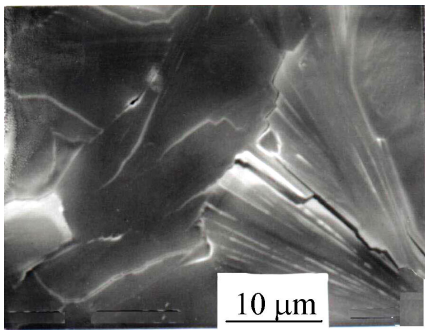

Figure 23. View of superficial bursts after exposition to β^- particle.

To conclude this model, chaos requires how the distribution of repulsor affects the dynamical characteristics in the phase portrait. A chaotic distribution corresponding to different types of perturbation is characterized by various aspects of derivatives. The problem is the complexity of instability in the phase space, making it difficult to interpret. In a fluctuating signal, if more is the chaotic state, more is the perturbation of the derivative for a non-stationary regime. The Lyapunov exponent and various derivatives are useful aids. In exploiting these, pseudo-prepassivity and pseudo-passivity are temporary situations. The worst situation is the breakdown of oxide. At this stage, the system becomes unstable. Therefore, the analysis of derivatives plays a role in studying phenomena generated by the dynamic system. This is complementary to the classical tests [31,32]. For models 3 and 4, there are too many β^- impacts to determine the influence of potential on the Lyapunov exponent. Therefore, the examination of the derivative as a function of time and the 3D divergence sector has been completed.

5. Model 3, Measurements for 6×10^7 Energetic Impacts cm^{-2} s^{-1}

5.1. Aspects of Global Spectra

In addition to model 2, model 3 corresponds to the progressive destruction of oxide evidenced by the concept of chaos mechanism. The β^- particle plays a key role in the

free electron energy being charged onto the active oxide via a physical diffusion process. The attraction between positively ionized pseudo-oxide and energetic negative electrons also produces the attack. Impact density and diffusion depend mainly on the free electron amount and the electronic structure of the active oxide. Although at low energy, this medium increases oxide degradation by the diffusion dense of β^- into oxide with no other protective barrier. Besides the physical diffusion of β^- particle, there is also the aspect of the charged low-energy compounds at the oxide surface forming activated OH^* complex accelerating the internal corrosion. Therefore, this adsorption and absorption can also be considered a quasi-substitution of OH^- favoring attack. In the context of crowding of β^- into oxide, the raw data associated with Figure 24 reinforces the idea of the correlative matrix to oscillate forming orbits as seen in A, B of Figure 25. It is difficult to interpret the chaotic aspect of these highly random data. However, it is possible to examine the instabilities. These consist of vectorizing three main scrolls extracted from the phase space (Figures 26–28 events 2 to 4). Sectorized scrolls correspond to steps activated by the β^- energy of oxide. In this case, the data was decomposed for a finite time to extrapolate the phenomena. However, this scheme should be used with caution. If the underlying system is chaotic, then the oxide breakdown has to lead to a good representation in topology to apprehend each chaotic repulsor. In Figures 27 and 28, event 2, the process is random, which means that long signals are repeated for an extensive range of potential passing or not in the origin of axes for a given set of parameters. Events 3 and 4 can be confused in the third quarter (Figure 27). In Figures 26–28, the double-loops resulting from β^- diffusion and adsorbed OH^* in oxide are not stabilized. This model is not passive, making it unstable (events 2 and 3). For basic information, according to these Figures, the energy distributed in the pseudo-oxide leads to breaking. Consequently, the brittle oxide produces localized corrosion, unlike conventional corrosion.

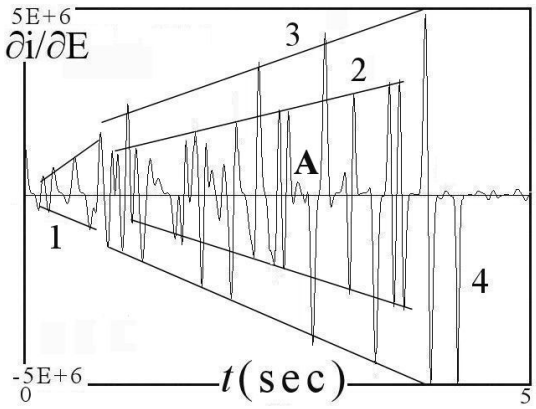

Figure 24. Instability for several events in the full range of potential.

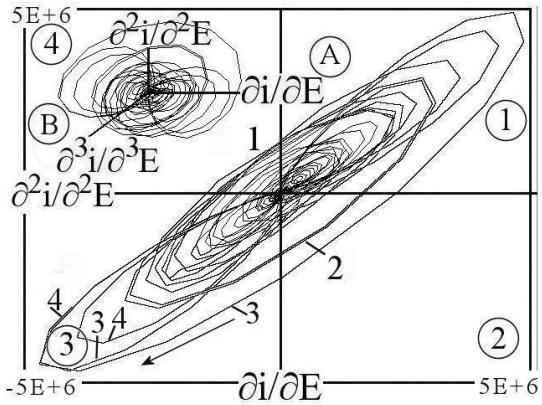

Figure 25. 2D and 3D views of phase space derivatives in all pseudo-passivity.

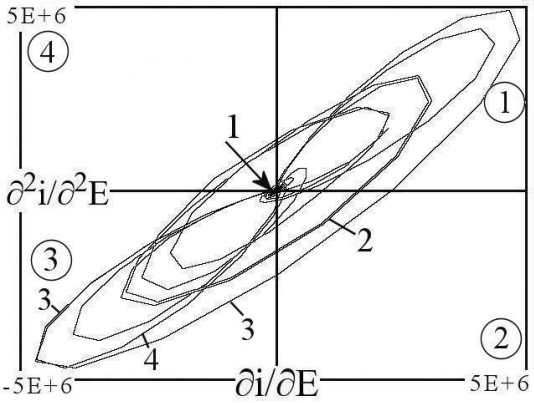

Figure 26. Phase-space derivatives, in the pseudo-passivity, 2.5-s passed the Flade potential, extended to 2.5-s.

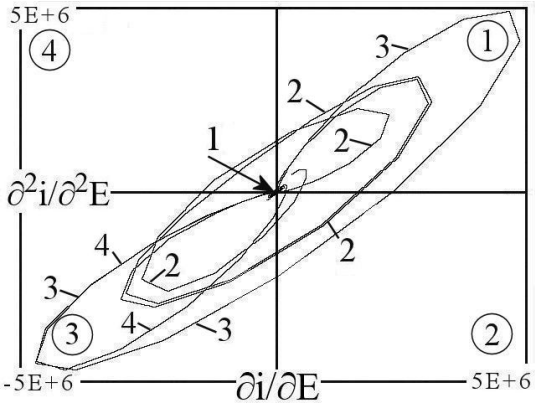

Figure 27. Phase-space derivatives, in the pseudo-passivity, 3-s passed the Flade potential extended to 2-s.

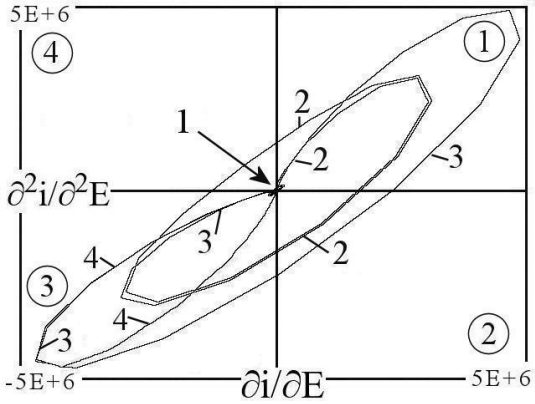

Figure 28. Phase-space derivatives, before the pseudo-transpassivity, 3.5-s passed the Flade potential extended to 1.5-s.

In Figure 24 events 2 and 3, the frequency measured for the major impacts varies randomly with time. It can be assumed that β^- energy modifies the structure of the oxide by breakdown, making it superficially sensitive to local corrosion. In the higher potential range, instabilities are substantial in the presence of this energy density. If the β^- energy and electron gap onto oxide exceed values, it can be expected that this environment contributes to stress and chaos. Since the attack of stainless steel depends on the equilibrium between pseudo-passivity and β^- energy, spectra oscillate and strongly correlate oxide balanced with activation. Stress is considered nucleate in producing more ionized oxide by bombarding

the β^- electron particle. This produces subsequent instability in a deterministic mechanism for oxide destruction. Considering the electrical schema in Figure 6, the predominant combination related to this electrochemical system is insertion combined with adsorption and unstable impedances [18]. Instabilities result from events with the rearrangement of the route in the chaotic orbits (Figure 25). This proves that the $\partial^2 i/\partial^2 E$ derivative has several module doubling routes making "eye" or elliptical excursions with a large negative loop at the transpassivity (event 4). Event 4 corresponds to oxygen adsorption linked with possible oxide destruction. The central orbits revolve around the nucleus, and this behavior corresponds to an attractor where nothing is exposed in the "eye" (Lyapunov exponent nil). However, it is noticed that the diverging points are responsible for connecting orbits in three modules (radionuclide adsorption, degraded oxide by β^-, and oxide destruction). These modules are evolutive and provide the three-phase space series. These are characterized by possible routes of unstable oxide.

Scrolls are due to the nucleation of these unstable activated oxides in the pseudo-passive potential associated with the propagating stress and oxide breakdown. The oxide stress occurs only for sufficient energy by the β^- particle. The phase space for the prominent instabilities is given in Figure 25. This Figure measures the complexity of the Lyapunov exponent when the trajectory diverges or converges. The lower value of convergence is placed near the "eye". According to the Figure and for the high values, the system is in an unstable configuration in the presence of activated adsorbate and large β^- energy. To better discern the chaos, examining the divergent random local (events 2 to 4) is interesting.

5.2. Aspects of Local Sectors in Spectra

As seen previously, the complex chaos intervenes in the phase space, so it applied short segment series at regular intervals to estimate the chaos level for an outcome domain. Therefore, well-chosen short segments are designed to extract chaotic parts. Effectively, a vector deciding the trajectory governs the phase space structure of a non-linear dynamical system. Based on these remarks, an analysis was compiled to study the local instability formed by activating β^- particles and energy released by decay. The advantage of this procedure is amenable to assembling the collected sectors, and this approach is relevant for any phase space in specific corrosion. Plotting segments provides a representation of the global or local dynamic. This reveals that the signals analyzed are of great interest to understanding how the attack is in non-regular or regular orbits. In particular, the signal through the invariant "eye" appears less important than the signal through the core or the orbit. Effectively, the equilibrium in the "eye" should be stable or meta-stable by restructuring oxide. These are indicators of oxide morphology. In Figures 29 and 30 A-B, spectra show the diversity of the divergence and convergence in the pseudo-passivity. Aspect in a front view indicates the oxide is perturbed and changing in pseudo-passivity for a 0.2-s extent. Chaotic dynamical systems of this type are invariably repulsive in the presence of β^- energy. Negative event 3 dominates the signal at 0.08-s (Figure 30). The same event also appears simultaneously in Figure 31 event 4 and Figure 32 event 3, corresponding to the beginning of pseudo-transpassivity. Figure 31 was obtained after a micro-pulse at 2.1-s passed the Flade potential (event A in Figure 24).

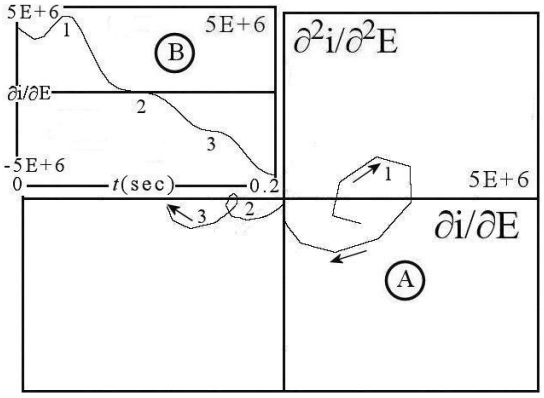

Figure 29. A: divergence sector, B: derivative in the function of time, 2.1-s passed the Flade potential, for the 0.2-s duration, Lyapunov exponent: 0.023 ± 0.139.

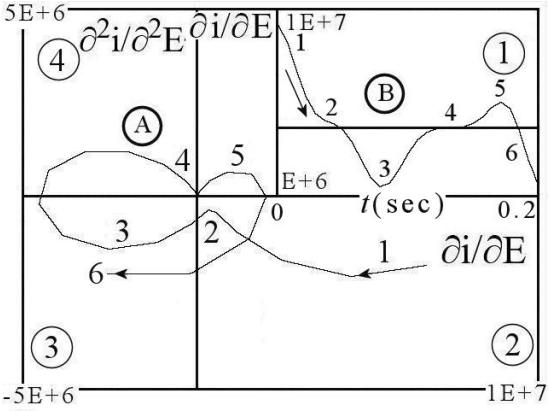

Figure 30. Divergence sector (A) and derivative in the function of time (B), 2.4-s passed the Flade potential, for the 0.2-s duration, Lyapunov exponent: 0.128 ± 0.525.

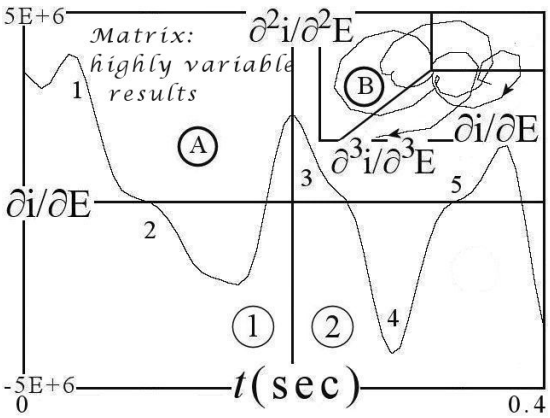

Figure 31. Derivative in the function of time (A) and diverging sector in 3D dimensions (B), 1: 2.1-s passed the Flade potential. 2: 2.4-s passed the Flade potential. For 0.2-s duration each. According to Figures 29 and 30. Lyapunov exponents: 0.427 ± 0.260.

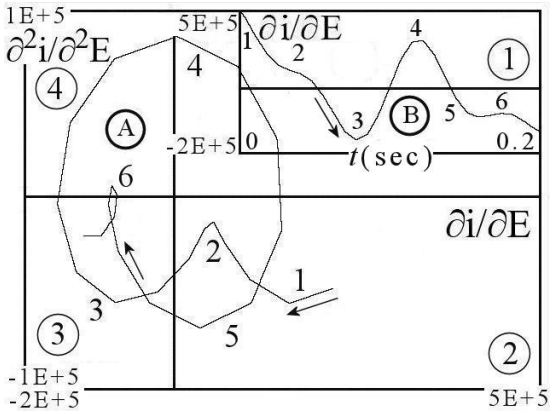

Figure 32. (A): Divergence sector, (B): Derivative in the function of time. At the beginning of pseudo-transpassivity, 3.8-s passed the Flade potential, for the 0.2-s duration, Lyapunov exponent: 0.403 ± 0.222.

These correspond to the same combination of these potentials. They indicate coherence between negative events in instabilities and local chaos spectra. Therefore, dynamic activation is responsible for multi-signals. Dynamic signals constitute sufficient proof of the presence of chaos. Such signals are evident even after the careful removal of spurious values. The existence of singular values on a chaotic repulsor involves serious interpretation problems, and it is difficult to obtain a suitable distribution. After the removal, dynamical systems in a chaotic regime fully reflect the properties of the oxide.

Then, the local signal can comfort results, and the previous figures show the fluctuating signal corresponding to a non-stationary state at a different time of the attack. An algorithm using a matrix function was applied in the chaos analyzer to detect the non-stationary signals, thereby oxide destruction. The goal of the chaos analyzer is also to predict the behavior of the model from a set of data. The equivalent noise in the series depends on the potential. Consequently, the phase space transform reveals distinct signatures ascribed to specific behaviors distinguishing chaos.

Figure 31 endorses the results modeled according to the 0.4-s signal to qualify the deviation in the phase space[33]. This technique brings out the concave (event 2) and convex (event 5) shapes corresponding to convergence and divergence. From these, it is possible to interpolate the local variation of the computed model as a function of the neighboring experimental data. Combining the chaos technique with the voltammetry curves makes it possible to capture this local variability. In these Figures, the trajectory of the second derivative does not always pass by the origin of axes, this signifies unstable overall oxide. Consequently, in this system, there is the shared action of the β^- energy and the pseudo-passive oxide on the local oxide destruction. When the β^- energy is enough to act, chaos is a continuously diverging dynamic system. The shape of the graphs discriminates the destruction of oxide. The chaotic oscillation and positive Lyapunov exponent increase signifying stress by increasing the pseudo-passive potential.

6. Model 4, Measurements for 6×10^8 Energetic Impacts cm^{-2} s^{-1}

6.1. Aspects of Global Spectra

After presenting the chaos results for low and medium content in low-energy radionuclides, the following experiments were realized at the β^- energy of 3.6 $\times$ 10^6 MeV cm^{-2} s^{-1}. In Figure 33, the instabilities are visible during the depassivation of oxide for 5-s, which confirms the disturbance on the high generalized attack found in voltammetry. The frequency measured for major impacts is 0.9 events per second, this does not increase with the number of impacts. Pulse size remains weak. It can be assumed that all the oxide is destroyed. Disturbance can be examined by sectoring the spectra. Chaos formed on oxide depassivation intervenes in events 1–6 of Figure 34. Negative event 7 corresponds to the pseudo-transpassive potential. Figures 34 and 35 are decomposed into two serials

(events 4 and 6) in the depassivation potential as in Figure 33. Regarding these two events, loops are more intense in event 4. These are interactive on the oxide perturbation and degradation. On this basis, the chaos spectrum combined with sectors provides a powerful tool for determining events responsible for a few more divergences.

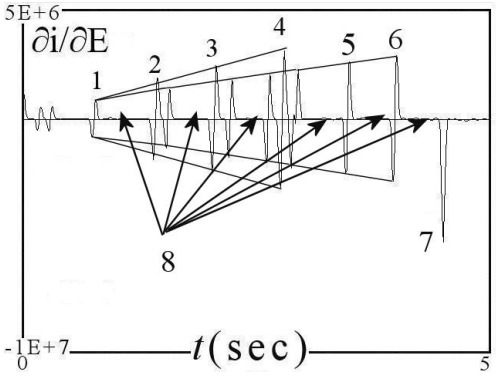

Figure 33. Instability for several events in the full range of potential, event 7: pseudo-transpassive potential.

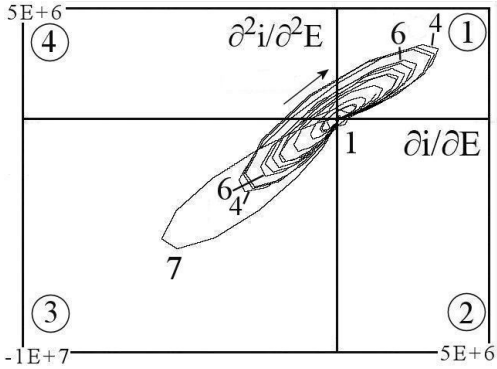

Figure 34. Phase space derivatives for oxide depassivation and pseudo-transpassive potential.

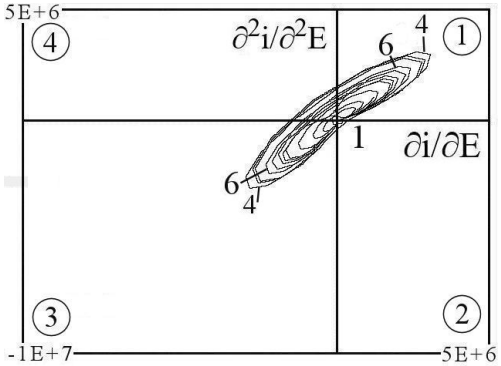

Figure 35. Phase space derivatives in depassivation, from the Flade potential, extended to 4.5-s.

The tendency of each sector is complex, and when attached, they entail multiple transforms of the dynamical system. This approach is amenable to efficient numerical computation in series showing instability (Figures 35 and 36). The electrochemical instability can be presumed to have been generated with a generalized attack (Figure 5). These events correspond to oxide rupture. Figure 36 shows that the trajectory suddenly diverges. This corresponds to the pseudo-transpassive potential. Then, the diverging trajectory converges, forming a toroid-presaging structural modification. These behaviors are difficult to interpret but correspond to the disappearance of the oxide. Consequently, this technique should

be valuable in exploring the 3D spectra for the dynamical system defined by the runs, and the approach is amenable to the destruction of oxide. The plotted serial results show it is reasonable to construct chaotic dynamical systems respecting the phase space structure. In such a case, this local approach helps highlight the chaos. The Lyapunov exponent increases with the potential signifying an unstable state in the core. The oxide is destroyed, leaving a generalized attack. In other words, the sectors should indicate diverging points where oxide no longer exists. This approach is valuable for examining the dynamics of chaos. The chaos analyzer and the voltammetry are good tools and agree to explicitly take into account the oxide degradation according to the experimental and simulated data.

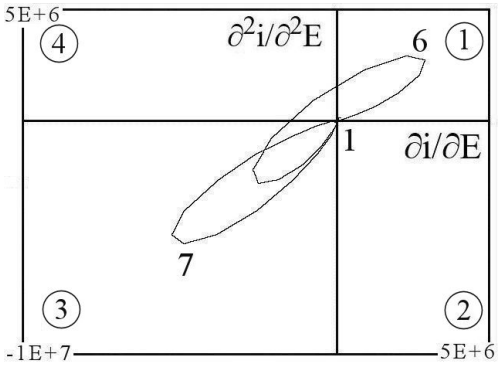

Figure 36. Phase space derivatives in the pseudo-transpassive potential, 3.8-s passed the Flade potential, extended to 1.2-s.

6.2. Aspects of Local Sectors in Spectra

In Figure 37, part A, the $\partial i/\partial E$ derivative in the function of time arises for 1.2-s passed the Flade potential. This distribution reveals a complex structure in oxide regarding the 3D dimensions for the local spectra (part B). This reflects the expansion of the phase space chaos. The disorder is attributed to the multi-absorption of β^- in the disturbed oxide volume. The diverging scroll is put in value in events 1 and 5 from the second derivative, which propagates for the third derivative. This is associated with the transformation of oxide. This evolution takes place through β^- penetration. Penetration changes the stability to lead to the destruction of oxide regarding the three dimensions. A change in oxide explains the signal obeying a random mechanism. In Figure 38, the positive Lyapunov exponents and the significant local signal in event 3 going an inaccurate origin of axes (parts A and B) define a false passivity. The same event is produced in Figure 39 for the perturbed events 2 and 4. In these Figures, the loops do not pass through the origin of the axes, making it possible to predict an unstable state. These obey the energy for oxide degradation by the strength of β^-. The electrochemical chaos model (Figure 6) can produce different scrolls of repulsors. This model respects the voltammetry curve for the charging energy via the β^- source.

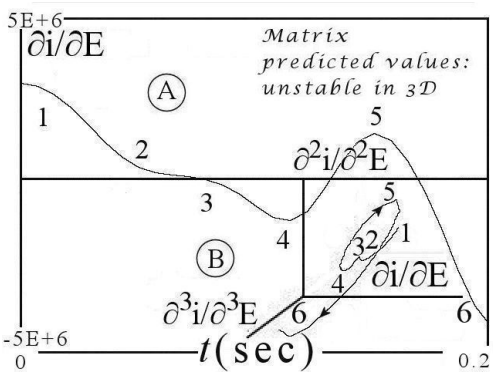

Figure 37. Derivative and local sector in 3D depending on time, 1.2-s passed the Flade potential, Lyapunov exponent: 0.167 ± 0.402.

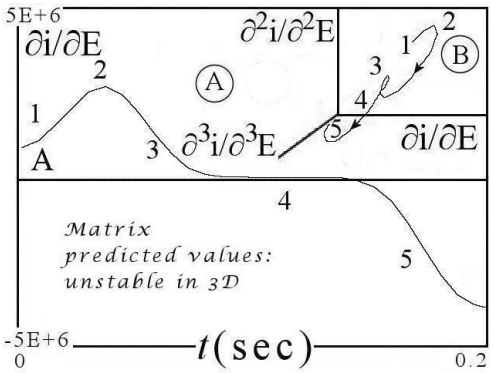

Figure 38. Derivative and local sector in 3D depending on time, 2.1-s passed the Flade potential, Lyapunov exponent: −0.034 ± 0.618.

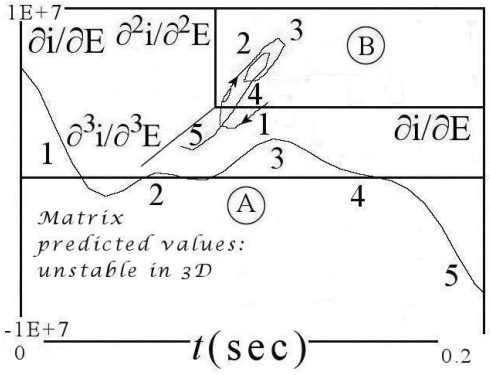

Figure 39. Derivative and local sector in 3D depending on time, 3.3-s passed the Flade potential, Lyapunov exponent: 0.449 ± 0.335.

In Figure 40, obtained in transpassivity, destruction dominates when oxide turns into a disintegration by the energy source, as seen for a more elongated positive derivative in the function of time (events 1, 2, and 5). Once the β^- energy source is high enough, oxide disintegration takes over as repulsive chaos. There is also a false stabilizing effect which may correspond to the absence of oxide (events 3–4). Since the system depends on the disturbance induced by β^- onto oxide degradation, the electrochemical mechanism strongly oscillates, as detailed in these Figures. These events should be due to the interfering action with the remaining oxide. The result is a period-doubling chaos route, as in Figure 33, where the instabilities are increasing. In this condition, the increasing Lyapunov exponent synchronizes chaos coupled with the β^- action so that there is progressive destruction.

Therefore, the response should be treated as a chaotic signal leading to the elimination of oxide (Figure 40 event 5). Due to the high instability and degradation of oxide, it is impossible to obtain a stable correlation matrix. Qualitatively, the divergence in the local phase space with low convergence in the core corroborates the electrochemical impedance (Figure 6). For that, B of Figure 40 shows the derivative spiraling (events 2–3) and the diverging points (events 4–5) in the questionable quarter. This derivative examined in the function of the time is located between two pulses (events 1 and 5). The converging intrusion in the core meets the balanced model. But as this state is resonant, it supports the idea of oxide destruction in Figure 40. In this sense, the local Lyapunov value always changing positively in the trajectory also signifies resonant oxide. Despite the negative values of the derivative in the function of time, the 3D topology matrix is fruitful in revealing the trajectory does not pass through the origin of axes meaning an intense unstable oxide. Therefore, in model 4, there is entire degradation of oxide. Destruction by the β^- energy, suggests a dynamic system unable to return to a stable point. The system cannot have an equilibrium. There is a random aspect with diverging points making the spiraled signal to be unstable.

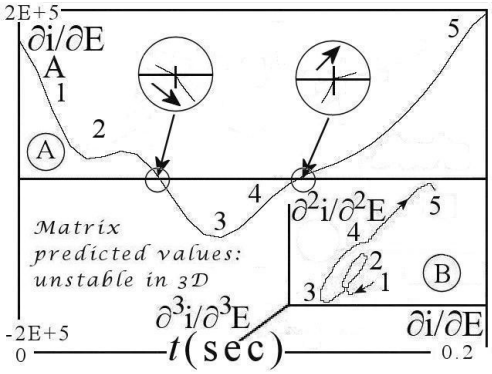

Figure 40. Derivative and local sector in 3D depending on time, in transpassivity, 5.0-s passed the Flade potential, Lyapunov exponent: 0.475 ± 0.281.

7. Conclusions

This research was conducted in tritiated water to determine the type of corrosion impacted by β^- low energy on the 316L stainless steel. According to the voltammograms realized in a glove-box and the signals computed from a chaos analyzer program, four models were examined for the attack. These correspond to the impact density of β^- onto the surface of the oxide. At the lowest impacts (lower energy of 10^3 MeV cm^{-2} s^{-1}), the response of the oxide layer indicates pseudo-passivity. In the relevant part at a few more impacts (energy of about 10^4 MeV cm^{-2} s^{-1}), the presence of chaos is highlighted. The third part (10^5 MeV cm^{-2} s^{-1}) shows numerous instabilities signifying unstable oxide, and the compilation of the signal values highlights irregularities in the chaos determinism with the dissipation of energy in the whole passivity domain. In this part, there is no more passivity. At the highest concentration of radionuclide, the impact density is very high (energy of 4×10^6 MeV cm^{-2} s^{-1}), which leads to the complete destruction of the oxide. The alloy is exposed and is no longer protected in the passivity domain. These results corroborate those obtained from the laser beam.

Funding: This research received no external funding.

Data Availability Statement: The data that support the findings of this study are available from the corresponding author upon reasonable request.

Conflicts of Interest: The author declares no conflict of interest.

References

1. Lässer, R. Tritium and helium-3 in metals. In *Materials Science*; Series in Materials Science; Springer: New York, NY, USA, 1989; Volume 9.
2. Oltra, R.; Boquillon, J.P. Depassivation by laser impacts. *Electrochim. Acta* **1986**, *31*, 869–872. [CrossRef]
3. Oltra, R.; Indrianjafy, G.M.; Efimov, I.O. Laser Pulsed Irradiation of Passive Films. In *Modifications of Passive Oxide*; Institute of Materials, T., Ed.; European Federation of Corrosion: Paris, France, 1993; Volume 12, pp. 230–233.
4. Arnoult, X.; Arnoult-Růžičková, M.; Maňák, J.; Viani, A.; Brajer, J.; Arrigoni, M.; Kolman, R.; Macák, J. Corrosion and Electrochemical Properties of Laser-Shock-Peening-Treated Stainless Steel AISI 304L in VVER Primary Water Environment. *Metals* **2022**, *12*, 1702. [CrossRef]
5. Kameo, Y.; Nakashima, M.; Hirabayashi, T. New laser decontamination technique for radioactively contaminated metal surfaces using acid-bearing sodium silicate gel. *J. Nucl. Sci. Technol.* **2004**, *41*, 919–924. [CrossRef]
6. Sentis, M.L.; Delaporte, P.; Marine, W.; Uteza, O. Surface oxide removal by a XeCl laser for decontamination. *Quantum Electron.* **2000**, *30*, 495–500. [CrossRef]
7. Delaporte, P.; Gastaud, M.; Marine, W.; Sentis, M.; Uteza, O.; Thouvenot, P.; Alcaraz, J.L.; Le Samedy, J.M.; Blin, D. Radioactive oxide removal by XeCl laser. *Appl. Surf. Sci.* **2002**, *197–198*, 826–830. [CrossRef]
8. Yoo, H.J.; Baek, S.; Kim, J.H.; Choi, J.; Kim, Y.J.; Park, C. Effect of laser surface cleaning of corroded 304L stainless steel on microstructure and mechanical properties. *J. Mater. Res. Technol.* **2022**, *16*, 373–385. [CrossRef]
9. Wang, X.; Wang, J.; Fu, C.; Gao, Y. Determination of corrosion type by wavelet-based fractal dimension from electrochemical noise. *Int. J. Electrochem. Sci.* **2013**, *8*, 7211–7222. [CrossRef]
10. Macía, L.F.; Tourwé, E.; Pintelon, R.; Hubin, A. A new modeling method for determining electrochemical parameters from LSV experiments using the stochastic noise. Part I: Theory and validation. *J. Electroanal. Chem.* **2013**, *690*, 127–135. [CrossRef]
11. Bellanger, G. Blocking Hydrogen Diffusion in Palladium Cathode I-Analyzed by Electrochemistry; II-Analyzed by Chaos. *Hydrogen* **2022**, *3*, 123–160. [CrossRef]
12. Li, X.; Liang, X.; Liu, D.; Chen, R.; Huang, F.; Wang, R.; Rettenmayr, M.; Su, Y.; Guo, J.; Fu, H. Design of (Nb, Mo)40Ti30Ni30 Alloy membranes for Combined Enhancement of Hydrogen Permeability and Embrittlement Resistance. *Nat. Sci. Rep.* **2017**, *7*, 209. [CrossRef]
13. Kurbanova, E.D.; Polukhin, V.A. Influence of Alloying Ti, Mo, Zr on Strength and Workability of Membrane Alloys (Nb-Ni, V-Ni). *Procedia Struct.* **2022**, *40*, 251–257. [CrossRef]
14. Bellanger, G. *Corrosion Induced by Low-Energy Radionuclides- Modeling of Tritium and Its Radiolytic and Decay Products Formed in Nuclear Installations, in Materials Science*; Elsevier Science: Amsterdam, The Netherlands, 2004.
15. Bellanger, G. Localized corrosion of 316L stainless steel in tritiated water containing aggressive radiolytic and decomposition products at different temperatures. *J. Nucl. Mater.* **2007**, *374*, 20–31. [CrossRef]
16. Sprott, J.C. *Chaos and Time*; Series Analysis; Oxford University Press: Oxford, UK, 2003.
17. Anishchenko, V.S.; Astakhov, V.; Neiman, A.; Vadivasova, T.; Schimansky-Geier, L. *Nonlinear Dynamics of Chaotic and Stochastic Systems—Tutorial and Modern Developments*; Springer: New York, NY, USA, 2007.
18. Muthuswamy, B. Implementing memristor based chaotic circuits. *Int. J. Bifurcat. Chaos* **2010**, *20*, 1335–1350. [CrossRef]
19. Cottis, R.; Turgoose, S. *Electrochemical Impedance and Noise*; Corrosion Testing Made Easy; Nace: Houston, TX, USA, 1999.
20. Petrzela, J. Chaos in Analog Electronic Circuits: Comprehensive Review, Solved Problems, Open Topics and Small Example. *J. Math.* **2022**, *10*, 4108. [CrossRef]
21. O'Connell, R.A. *An Exploration of Chaos in Electrical Circuits*; Senior Projects Spring; Bard College: Baltimore, MA, USA, 2016.
22. Marquardt, R.; Zahari, F.; Carstensen, J.; Popkirov, G.; Gronenberg, O.; Kolhatkar, G.; Kohlstedt, H.; Ziegler, M. *Advanced Electronic Materials, Impedance Spectroscopy on Hafnium Oxide-Based Memristive Devices*; Wiley, Online Library: Hoboken, NJ, USA, 2023. [CrossRef]
23. Zhong, G.Q.; Ayrom, F. Periodicity and chaos circuit. *IEEE Trans. Circuits Syst.* **1985**, *32*, 501–503. [CrossRef]
24. Chua, L.O.; Lin, G.N. Intermittency in a piecewise-linear circuit. *IEEE Trans. Circuits Syst.* **1991**, *38*, 510–520. [CrossRef]
25. Xia, D.; Song, S.; Wang, J.; Shi, J.; Bi, H.; Gao, Z. Determination of corrosion types from electrochemical noise by phase space reconstruction theory. *Electrochem. Commun.* **2012**, *15*, 88–92. [CrossRef]
26. García, E.; Hernández, M.A.; Rodríguez, F.J.; Genescá, J.; Boerio, F.J. Oscillation and Chaos in Pitting Corrosion of Steel. *Corrosion* **2003**, *59*, 50–58. [CrossRef]
27. Bartissol, P.; Chua, L.O. The double hook. *IEEE Trans. Circuits Syst.* **1988**, *35*, 1512–1522. [CrossRef]
28. Wigdorowitz, B.; Petrick, M.H. Modelling concepts arising from an investigation into a chaotic system. *Math. Comput. Model. Dyn. Syst.* **1991**, *15*, 1–16. [CrossRef]
29. Limphodaen, N.; Chansangiam, P. Mathematical analysis for classical Chua circuit with two nonlinear resistors. *Songklanakarin J. Sci. Technol.* **2020**, *42*, 678–687. [CrossRef]
30. Cheng, W.; Luo, S.; Chen, Y. Use of EIS, Polarization and electrochemical noise measurements to monitor the copper corrosion in chloride media at different temperatures. *Int. J. Electrochem.* **2019**, *14*, 4254 – 4263. [CrossRef]
31. Anishchenko, V.S.; Vadivasova, T.E.; Okrokvertskhov, G.A.; Strelkova, G. Correlation analysis of dynamical chaos. *Phys. A* **2003**, *325*, 199–212. [CrossRef]

32. Le Maıtre, O.P.; Reagan, M.T.; Najm, H.N.; Ghanem, R.G.; Knio, O.M. A stochastic projection method for fluid flow. ii. Random process. *J. Comp. Phys.* **2002**, *181*, 9–44. [CrossRef]
33. Blatman, G.; Sudret, B. Adaptive sparse polynomial chaos expansion based on least angle regression. *J. Comput. Phys.* **2011**, *230*, 2345–2367. [CrossRef]